Peeking into pit fields - A new model of secondary plasmodesmata formation

The Plant Cell, Vol. 20: 1504–1518, June 2008, www.plantcell.org © 2008 American Society of Plant Biologists

Peeking into Pit Fields: A Multiple Twinning Model of Secondary Plasmodesmata Formation in Tobacco [W]

Christine Faulkner,[a] Ozgur E. Akman,[b] Karen Bell,[a] Chris Jeffree,[a] and Karl Oparka[a,1]

[a] Institute of Molecular Plant Sciences, School of Biological Sciences, University of Edinburgh, Edinburgh EH9 3JH, United Kingdom

[b] Centre for Systems Biology at Edinburgh, University of Edinburgh, Edinburgh EH9 3JH, United Kingdom

In higher plants, plasmodesmata (PD) are major conduits for cell–cell communication. Primary PD are laid down at cytokinesis, while secondary PD arise during wall extension. During leaf development, the basal cell walls of trichomes extend radially without division, providing a convenient system for studying the origin of secondary PD. We devised a simple freeze-fracture protocol for examining large numbers of PD in surface view. In the postcytokinetic wall, simple PD were distributed randomly. As the wall extended, PD became twinned at the cell periphery. Additional secondary pores were inserted at right angles to these, giving rise to pit fields composed of several paired PD. During wall extension, the number of PD increased fivefold due to the insertion of secondary PD. Our data are consistent with a model in which a subset of the original primary PD pores function as templates for the insertion of new secondary PD, spatially fixing the position of future pit fields. Many of the new PD shared the same wall collar as the original PD pore, suggesting that new PD pores may arise by fissions of existing PD progenitors. Different models of secondary PD formation are discussed. Our data are supported by a computational model, Plasmodesmap, which accurately simulates the formation of radial pit fields during cell wall extension based on the occurrence of multiple PD twinning events in the cell wall. The model predicts PD distributions with striking resemblance to those seen on fractured wall faces.

INTRODUCTION

Plasmodesmata (PD), the small pores that interconnect plant cells, are difficult to image due to their inaccessibility and sensitivity to damage (reviewed in Roberts and Oparka, 2003). Primary PD are laid down at cytokinesis by entrapment of endoplasmic reticulum (ER) strands between enlarging Golgi-derived vesicles (Hepler, 1982). These PD have a simple architecture, comprising a single plasma membrane–lined pore containing an axial desmotubule connected to the cortical ER network (Overall and Blackman, 1996; Oparka, 2004). The desmotubule is separated from the plasma membrane by a cytoplasmic sleeve through which both endogenous signals (Lucas and Lee, 2004) and viral genomes (Lucas, 2006) are thought to pass. Simple PD may be surrounded by a specialized raised wall collar that differs in composition from the cellulose wall (Olesen, 1979; Badelt et al., 1994; Turner et al., 1994). The origins of PD that are inserted secondarily into the expanding plant cell wall (i.e., postcytokinetically) remains enigmatic, and recent reviews of wall growth do not consider the formation of secondary PD (e.g., Baskin, 2005; Cosgrove, 2005).

In the course of leaf development, simple primary PD give way to branched structures during the sink–source transition (Ding et al., 1992a; Oparka et al., 1999; Ehlers and Kollmann, 2001; Roberts et al., 2001), and the PD size exclusion limit is downregulated, indicating that simple and branched PD differ in both structure and function (Oparka et al., 1999). Simple and branched PD also interact differently with viral movement proteins (MPs), intercellular chaperones that traffic viral genomes between cells (Oparka, 2004; Lucas, 2006). For example, MPs from diverse viral groups accumulate exclusively in the central cavities of branched PD (reviewed in Lucas, 2006). MP accumulation occurs independently of other viral factors and can be seen in transgenic plants that constitutively express viral MPs (Ding et al., 1992a; Roberts et al., 2001). Recently, the accumulation of viral MP in central cavities has been used to isolate proteins specifically associated with branched PD (Kishi-Kaboshi et al., 2005).

For many higher plants, the density of PD per shared wall interface remains relatively constant during wall extension due to the insertion of new secondary PD (Seagull, 1983). Although the number of PD is maintained, there is a clear shift in PD distribution from random PD to aggregated PD located in distinct pit fields (Seagull, 1983; Barnett, 1987). Several authors have reported the formation of apparent H-shaped intermediates thought to be the precursors of branched PD (Ding et al., 1992a; Itaya et al., 1998; Oparka et al., 1999; Ehlers and Kollmann, 2001), possibly arising as fusions of existing simple PD by selective removal of wall in the region of the middle lamella (Ding et al., 1992a; Ding and Lucas, 1996). Other models have suggested that Golgi-derived deposition of new wall materials occurs between adjacent PD leading to entrapment of new cortical ER profiles into the thickening cell wall (reviewed in

[1] Address correspondence to karl.oparka@ed.ac.uk.
The author responsible for distribution of materials integral to the findings presented in this article in accordance with the policy described in the Instructions for Authors (www.plantcell.org) is: Karl Oparka (karl.oparka@ed.ac.uk).

[W] Online version contains Web-only data.

www.plantcell.org/cgi/doi/10.1105/tpc.107.056903

Ehlers and Kollmann, 2001). Some PD arise entirely de novo across unrelated wall interfaces, for example, in graft unions, chimeras, protoplast fusions, and host-pathogen interfaces (reviewed in Ehlers and Kollmann, 2001). There has been considerable debate as to whether the PD pores that arise postcytokinetically during wall development should be considered as true secondary PD or as modified primary PD (Ehlers and Kollmann, 2001). Strictly speaking, any new PD pore that arises postcytokinetically is secondary in origin (Barnett, 1987); therefore, the term secondary PD will be used here to describe all new PD pores that were not present at cytokinesis.

In most plant tissues, PD are usually seen in longitudinal views but are difficult to image. Surface views of PD are rare and occur by chance when glancing sections of wall pass through the neck of the PD pore (e.g., Burgess, 1971; Seagull, 1983; Robinson-Beers and Evert, 1991; Ding et al., 1992b). Such views have revealed some of the greatest detail of PD substructure (Robinson-Beers and Evert, 1991; Ding et al., 1992b; Overall and Blackman, 1996), showing globular proteins associated with the central desmotubule and PM and spoke-like structures connecting the desmotubule with the PM (Overall and Blackman, 1996; Oparka, 2004). One of the major problems in studying the pattern of secondary PD formation is a lack of suitable techniques for exposing them on a single wall interface. Furthermore, most cells in developing tissues undergo subsequent mitotic divisions giving rise to new populations of primary PD that are difficult to distinguish from secondary PD (Ehlers and Kollmann, 2001). The growing interest in novel PD proteins (Faulkner et al., 2005; Sagi et al., 2005; Levy et al., 2007; Thomas et al., 2008), and in the structure/function relations of PD (Oparka, 2004), prompted us to explore new methods for imaging PD.

Tobacco leaf trichomes form at right angles to the leaf surface and arise from single epidermal cells. The cell wall that connects the large basal trichome cell with the underlying epidermis contains numerous PD (Waigmann et al., 1997; Roberts et al., 2001), and subsequent divisions of the trichome initials give rise to a chain of cells that contain PD in their adjoining walls but not in surface walls (Roberts et al., 2001). This arrangement of PD makes the leaf trichome an attractive model for studies of PD functions (Derrick et al., 1992; Oparka and Prior, 1992; Waigmann and Zambryski, 1995, 2000; Angell et al., 1996; Waigmann et al., 1997). During development, the basal trichome wall undergoes massive radial extension without subsequent division, forming an interface that contains the primary PD laid down at cytokinesis as well as the secondary PD deposited during wall extension (Roberts et al., 2001). To expose this entire wall interface for imaging and immunocytochemistry, we developed a simple freeze-fracturing protocol that shears the basal trichome cell from the underlying epidermis, exposing all PD and the proteins associated with them in surface view. This approach allows correlative imaging of PD with both confocal and high-resolution field emission electron microscopy (FESEM) and provides a facile means of imaging large populations of PD across a single shared interface.

Here, we show that the primary PD laid down at cytokinesis are distributed randomly across the cell plate. As the wall extends radially, new postcytokinetic PD are added immediately adjacent to existing PD, giving rise to discrete pit fields that contain a plethora of PD pairs. Eventually, all PD progeny undergo twinning, resulting in the formation of several paired PD within a single pit field. We discuss different models of secondary PD biogenesis and present a computational model of secondary PD development, Plasmodesmap, which accurately predicts the formation of discrete pit fields containing multiply paired PD.

RESULTS

To facilitate imaging of PD, we used a transgenic tobacco (*Nicotiana tabacum*) line in which the viral MP of *Tobacco mosaic virus* fused to green fluorescent protein (MP-GFP) is located within the central cavity of branched PD (Roberts et al., 2001). In this line, fluorescent PD are clearly visible in the end walls that interconnect trichome cells (Figure 1A). Developing tobacco leaves display two predominant types of trichome: small prostrate trichomes and large secreting glandular trichomes with bulbous apical cells (Figure 1B; see also Glover and Martin, 2000; Waigmann and Zambryski, 2000). Following freezing, the trichomes were removed by two methods (Figure 1D). In the first, a scalpel was used to gently brush the leaf parallel to the adaxial surface. Examination of leaves of different sizes revealed a range of fracture planes across the trichomes. The small prostrate trichomes were not fractured by this process due to their close proximity to the leaf epidermis (data not shown). However, in developing sink leaves of ~1.5 to 3.0 cm in length, fractures of the larger trichomes occurred consistently across the wall between the basal cell of the trichome and the underlying epidermis (Figure 1D), allowing PD to be imaged in face view. At this stage of leaf development, trichomes of several diameters were present, the majority of the developing trichomes falling in the size range of 15 to 80 μm in diameter (Figure 1B; see Supplemental Figure 1 online). In the second method, the trichomes were fractured by embedding the adaxial leaf surface in colloidal graphite prior to plunge freezing. Insertion of a scalpel blade parallel to the leaf surface removed the adaxial epidermis, leaving the fractured trichome basal cells exposed in the frozen graphite (Figure 1D).

Correlative Imaging of PD

Following fracturing, the exposed basal walls of trichomes were imaged by confocal laser scanning microscopy (CLSM) and FESEM (Figures 1 to 4). Calcofluor stained the exposed wall surface and revealed the development of discrete pit fields within which cellulose staining was completely absent. These pit fields were oriented in the direction of wall extension and increased in size from the center to the periphery of the extending cell wall (Figures 1F, 1G, 4D, and 5M). Fractures of trichomes expressing MP-GFP showed punctate fluorescence associated with aggregates of PD within the expanding pit fields, with an increased density of MP-GFP toward the perimeter of the expanding cell wall (Figures 1F and 4D). Immunostaining of the fractured wall face with LM6, an antibody to pectin (Willats et al., 1998; Orfila and Knox, 2000), revealed the pectin-rich nature of the pit fields (Figure 1G) and produced staining within the regions of wall that were unstained with Calcofluor.

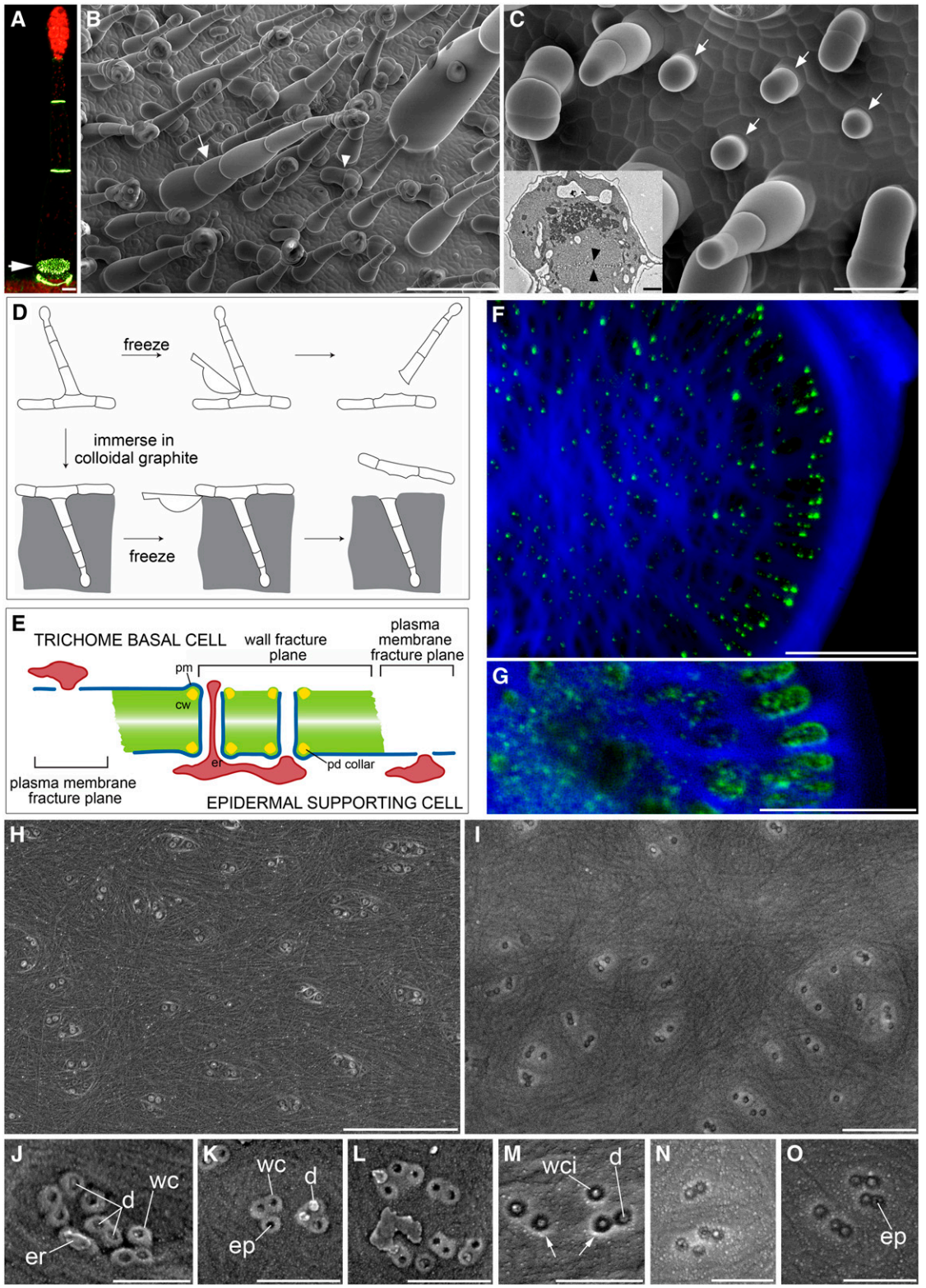

Figure 1. Freeze Fracturing of *N. tabacum* Leaf Trichomes.

(A) Transgenic tobacco line expressing an MP-GFP fusion reveals the location of MP-targeted PD connecting the end walls of trichome cells. The basal trichome cell wall is indicated (arrow). MP-GFP is shown in green and chlorophyll autofluorescence in red. Bar = 20 μm.

Our fracturing protocols allowed us to image three distinct views of PD in the basal trichome cell wall, shown diagrammatically in Figure 1E. When the fractured adaxial leaf surface was viewed, the most common fracture plane occurred close to the neck of PD, removing the upper plasma membrane (PM) and revealing distinct raised wall collars around the PD pores (Figures 1H, 1J to 1L, 2C, and 2D). In such cases, wall microfibrils were also revealed on the exposed face of the basal trichome cell (e.g., Figures 1H, 2C, and 2D). Examination of the exposed proximal PM face underlying the basal cell wall or the upper (distal) PM adjacent to the trichome wall (Figures 1I and 1M to 1O) revealed details of the PD neck region and its connection with the PM. At higher magnification, PD were seen clearly within the cell wall and also in the exposed PM connecting the trichome wall to the epidermis or the trichome (Figures 1I and 1M to 1O). Within the wall, various details were seen within individual PD. In many instances, the central desmotubule was located within the pore (Figures 1J to 1L). In others, the neck of the PD pore was obscured with membrane (Figures 1J to 1L), suggesting that the fracture had left the desmotubule anchored to a small piece of cortical ER attached to the neck of the pore. More rarely, the pore appeared as an empty tube, probably resulting from removal of the desmotubule and associated ER during fracturing (Figures 1J to 1L). In most cases, a circular ring was observed around the PD pore that we interpret as an imprint of the wall collar at the point of its contact with the PM (Figures 1I and 1M to 1O). An outer ring of membrane, lighter in shade than the wall collar, was also observed around the collar imprint (Figures 1I and 1M to 1O). Such fractures across the PM face showed that the openings of the PD were obscured by membranous caps derived from the underlying cortical ER covering the PD orifice (Figures 1I and 1M to 1O, with a diagram in Figure 1E). This latter fracture plane gives an unusual view of PD looking from the interior of the PD into the underlying cell. The fractured PM face also showed imprints of the cellulose microfibrils that were removed from this interface during fracturing (Figures 1I and 2E). These distinct views of PD allowed us to compare the distributions of PD leading into both the proximal and distal faces of the basal cell wall (Figures 1 and 2).

Changes in PD Distribution during Wall Extension

Trichomes are derived from an anticlinal divison of an epidermal cell when the latter reaches a diameter of ~10 μm (Figure 1C). In the newly formed trichome wall, simple PD were distributed randomly (Figures 2A and 2B). In larger basal trichome walls (20 to 30 μm in diameter), we noticed the appearance of a zone of PD at the cell perimeter in which virtually all the PD profiles were closely paired (Figures 2D and 2E). These PD twins were mostly oriented parallel to cellulose microfibrils, that is, in the radial plane of extension (Figure 2E). PD twins were observed not only in the wall fracture plane, but also in both the epidermal and trichome basal cell PMs, indicating that the pores were twinned along their entire length through the adjoining wall. In Figure 2E, several twinned PD are seen on the distal PM face. Note that many of these PD pores appear dumbbell shaped in surface fracture, indicating that two closely adjacent PD may share a single wall collar or even orifice. Thin sectioning of walls stained with zinc iodide osmium (ZIO) also revealed the twinned PD in longitudinal profiles (Figures 2F to 2J).

To derive distribution data for PD across a single wall interface, multiple images taken on the FESEM at magnifications of 13 to 15K were montaged, allowing the positions of individual PD to be recorded. The data in Figure 3 show transects across single walls of trichomes of increasing diameters, with the positions of individual PD indicated. The distributions of ~9000 PD were mapped onto transects of entire wall faces of trichomes ranging from 15 to 85 μm in diameter. The total number of PD in the trichome basal wall increased approximately fivefold during wall extension, from ~500 to 2500 PD per shared wall interface (Figure 3A). In small trichomes (15 to 20 μm in diameter), we

Figure 1. (continued).

(B) Scanning electron micrograph showing the distribution of trichomes across the adaxial surface of a 2.5-cm-long leaf. A range of secretory trichomes is present. Large secretory trichomes (arrow) are distinguishable from smaller prostrate trichomes (arrowhead). Bar = 150 μm.

(C) Leaf trichomes emerge from single epidermal cells. The main picture shows a scanning electron micrograph of a young leaf surface with emerging trichomes indicated with arrows. The inset shows a transmission electron micrograph of the developing cell plate between the basal trichome cell and the epidermis (arrowheads). Bar = 50 μm.

(D) Schematic showing the fracturing protocols employed for trichome removal.

(E) Fracture planes observed in the basal trichome wall. cw, cell wall.

(F) Fractured basal wall of an MP-GFP trichome counterstained with Calcofluor white to reveal cellulose (blue). MP-GFP (green) associated with PD occurs in unstained (cellulose-deficient) pit fields in the cell wall. Bar = 20 μm.

(G) Staining of pectin (green) within pit fields with the pectin-specific antibody LM6. Cellulose staining with calcofluor is shown in blue. Bar = 20 μm.

(H) Fractured basal wall of an MP-GFP trichome imaged by FESEM. PD appear surrounded by raised wall collars. Cellulose microfibrils are visible on the surface of the wall. Bar = 2 μm.

(I) Detail of the PM fracture surface. Wall microfibrils are seen as negative imprints. Bar = 1 μm.

(J) Group of 11 PD pores showing prominent wall collars (wc) around the pores and desmotubules (d) within the pores. In some cases, a small piece of cortical ER covers the pore orifices. Bar = 0.5 μm.

(K) Group of PD showing pores with attached desmotubules and other pores that appear empty (ep; see **[E]** for orientation) due to removal of the desmotubule during fracturing. wc, wall collar; d, desmotubule. Bar = 0.5 μm.

(L) As in **(K)** but showing remnants of cortical ER associated with the necks of the pores. Bar = 0.5 μm.

(M) to **(O)** PM fracture faces showing ER caps from the underlying cell associated with the neck of the PD pores and imprints of the wall collars (wci) on the PM surface. A ring of membrane, lighter in shade than the wall collar, is also visible around the wall collar imprints (arrows). d, desmotubule; ep, empty pore. Bar = 0.5 μm.

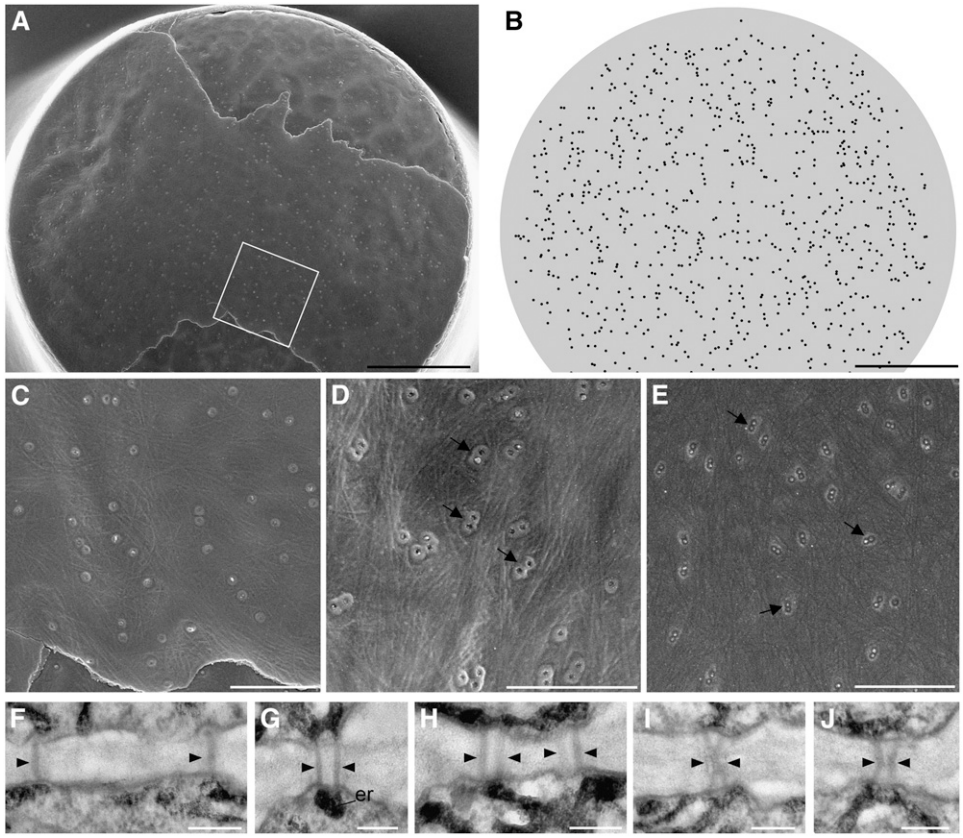

Figure 2. PD in the Basal Trichome Wall.

(A) Fracture of the postcytokinetic cell plate, revealing fracture planes across both the wall and PM interfaces. Details of the boxed region are shown in **(C)**. Bar = 5 μm.
(B) PD locations of the trichome shown in **(A)** are mapped as black spots on the gray wall area. PD are randomly distributed. Bar = 5 μm.
(C) Boxed region from **(A)** showing mostly discrete PD in the cell wall plane. Bar = 1 μm.
(D) Twinned PD (arrows) visible in the cell wall fracture plane. Bar = 1 μm.
(E) Twinned PD (arrows) visible in the PM fracture plane. Bar = 1 μm.
(F) to **(J)** Twinned PD profiles viewed after ZIO fixation and thin sectioning. The electron-dense stain has accumulated in the cortical ER at the neck of the PD pores (arrowheads). Twinned PD profiles are shown in **(I)** and **(J)**. Bar = 200 nm.

observed PD densities of ~2.5 PD per μm^2 of shared wall interface (see also Figure 2B), which fell to 0.5 PD μm^{-2} in trichomes of larger diameter (up to 80 μm; Figure 3B).

Extending radially from the cell center in larger trichomes, the frequency of PD pairs decreased, while the frequency of triplets and quadruplets increased (Figure 3). Most of these new PD were inserted in direct contact with existing PD, reflected by an increased percentage of contacting PD toward the perimeter of the cell wall (Figure 3C) and an increased density of PD toward the trichome edge (see Supplemental Figure 2 online). When the collars of three PD pores were in contact, the arrangement was frequently such that two pores were in the radial plane and the third was perpendicular to the other two (as opposed to forming a radial chain). Also, when more than two PD were present in an aggregate, they usually appeared in a hollow depression in the cellulose wall, suggesting the initiation of a pit field. As the number of PD in a pit field increased, the pattern of paired PD pores was maintained, giving rise to as many as 12 paired PD within a pit field (Figure 4A). While single PD pores were occasionally detected outside the pit fields, we were unable to determine whether these were primary PD sites that had failed to produce new PD or whether these pores had formed de novo across the cellulose region of wall. In larger trichomes (40 to 60 μm), the number of PD pores continued to increase within the pit fields (Figures 4A to 4C), most of them remaining as clearly distinguishable pairs (Figures 4A and 4B). In many of these larger trichomes, new cellulose microfibrils were deposited obliquely across the existing pit fields, subdividing them into smaller subgroups of paired PD (Figures 4B and 4C). With continued wall extension, the oblique bands of cellulose became larger (Figures 4D and 4E) and increasingly reinforced, eventually dividing the pit fields into discrete radial units.

Formation of Central Cavities

To examine the formation of central cavities in PD, we used transmission electron microscopy (TEM) coupled to an examination of

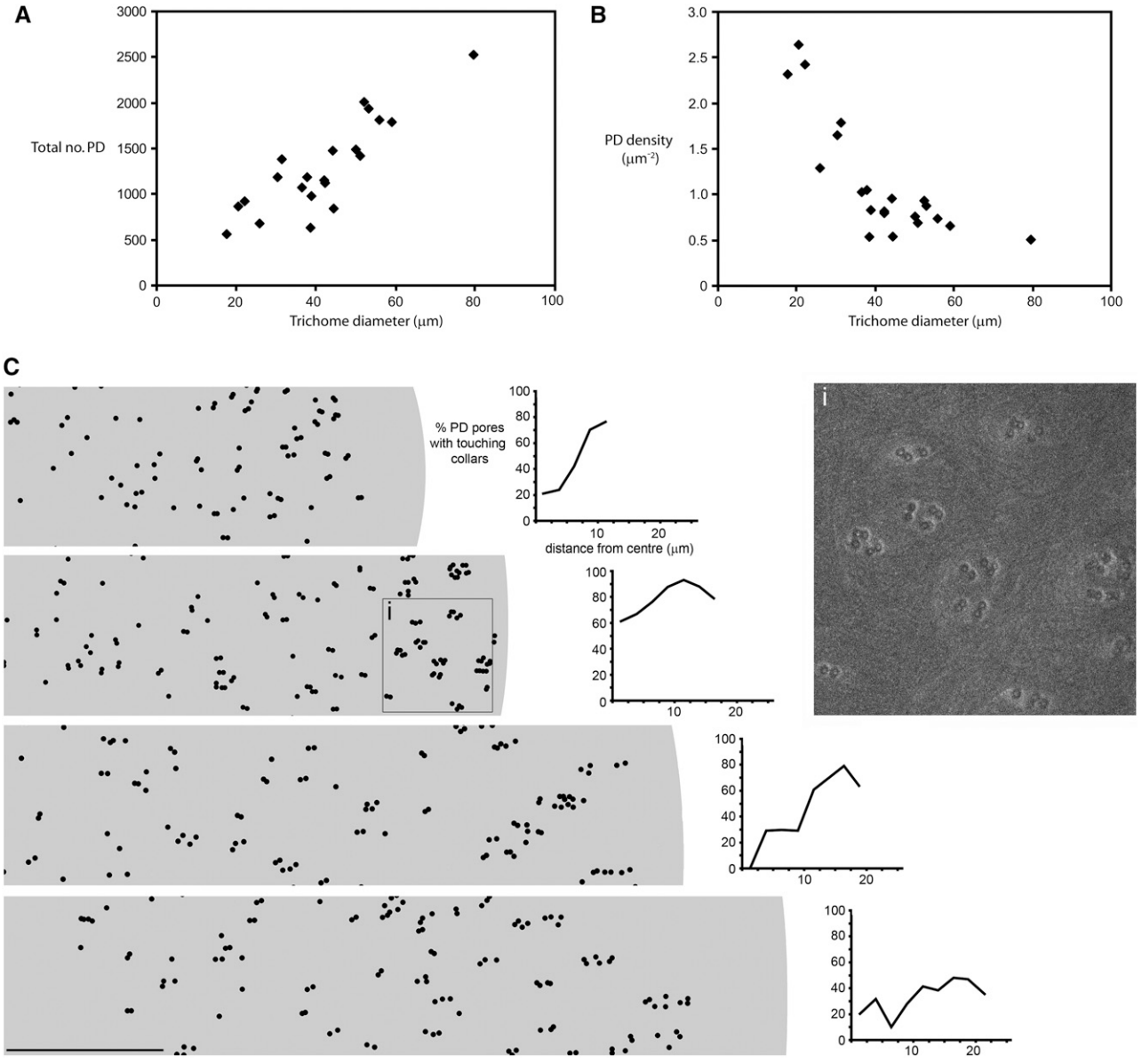

Figure 3. PD Distributions in Trichome Basal Cell Walls.

(A) Relationship between trichome diameter and total number of PD per wall interface. Total number of PD per wall face increases with trichome diameter.

(B) Relationship between trichome diameter and PD density. PD density is inversely proportional to trichome diameter.

(C) Mapped positions of PD in FESEM transects of trichome walls of increasing diameter (bar = 5 μm). Graphs show the proportion of PD with contacting collars increasing from the center to the edge of the cell wall. The inset (i) shows the boxed region indicated in the second transect. Note the increased clustering of PD pores toward the perimeter of the extending cell wall.

the distribution of MP-GFP, shown previously to accumulate in the central cavity of branched PD (Roberts et al., 2001). As expected, PD in newly formed trichome walls had a simple architecture (Figure 5A). In extending trichome walls, many of the PD pores were paired, as shown in Figures 2F and 2J. Following the extensive pairing of PD pores, many but not all of the twinned pores showed a central connection in the region of the middle lamella (Figures 5B and 5C). With continued wall extension, this central region expanded outward from the middle lamella forming a discrete cavity (Figures 5D and 7A). This situation was observed also in glancing sections of the basal trichome wall. At the neck region of the paired PD, the pores appeared as single channels surrounded by electron-dense wall collars (Figure 5E). Sections deeper in the wall, below the collars, revealed that many of the twinned pores were connected (Figure 5F). In large pit fields, groups of PD appeared to be separated by oblique bands

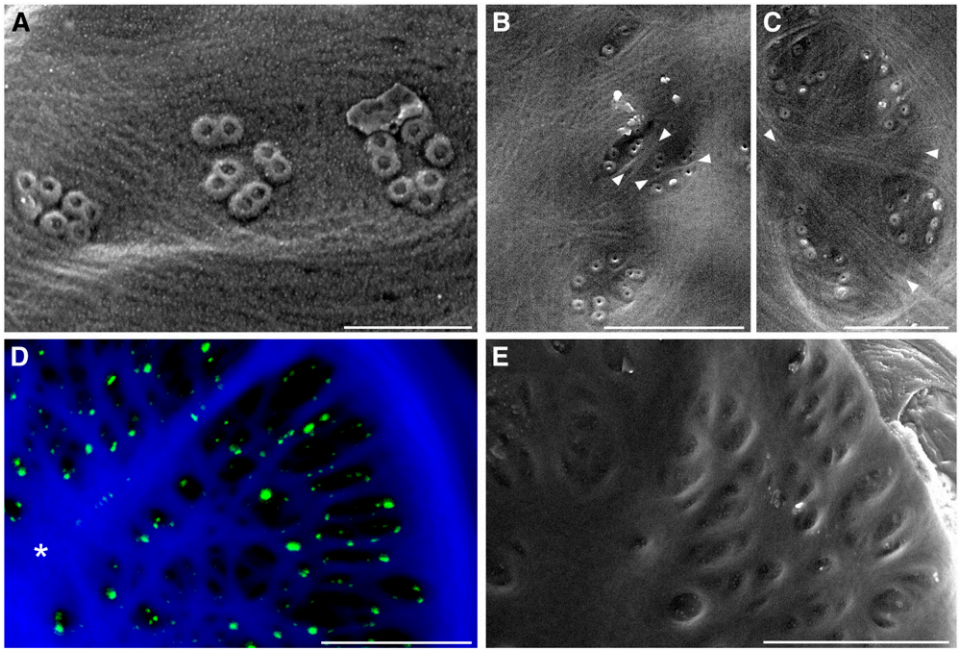

Figure 4. Correlative FESEM and CLSM Imaging of PD Pit Fields.

(A) PD within a single pit field are separated into three distinct groups. Note that PD remain closely twinned within the groupings. Bar = 0.5 μm.
(B) and **(C)** Subdivision of PD within pit fields by oblique insertion of cellulose microfibrils (arrowheads). Bar = 1.5 μm.
(D) and **(E)** Large basal cell walls showing prominent pit fields separated by new cell wall. **(D)** is a confocal laser scanning microscope projection of a fractured trichome wall stained with calcofluor (blue) to show cellulose. Note the extensive labeling of PD by MP-GFP (green) and the absence of PD from regions of wall connected to the walls between underlying epidermal cells (asterisk). **(E)** is a scanning electron micrograph of a fractured trichome wall showing the pit fields as sunken regions between the cellulose. Bars = 10 μm.

of cellulose (Figure 5G), consistent with FESEM observations (c.f. Figures 4D and 4E). In mature trichomes, many of the pores in a pit field were connected by central cavities. Glancing sections through the mid region of the wall revealed the extensive nature of the central cavities (Figures 5H and 5I), while immunogold labeling revealed the presence of MP-GFP (Figure 5I). We noticed that not all PD pores in a pit field were connected to one large cavity. Rather, subsets of pores appeared to be connected to cavities separated by discrete wall septa (Figures 5I and 5J). From TEM alone we were unable to determine whether all new pores became immediately connected to enlarging central cavities or whether the pores became connected subsequently as the cavities enlarged.

To image spatially the targeting of PD by MP-GFP, trichomes were fractured at different developmental stages and counterstained to reveal cellulose. To reveal the positions of PD in these trichomes, we immunostained the fractured wall faces with antibodies to calreticulin (Baluska et al., 1999) or callose (Oparka et al., 1997), both components of the neck region of the PD pore (Figures 5J and 5K). MP-GFP was first detected at the most distal point of the large peripheral pit fields (Figure 5J) and proceeded centripetally toward the center of the original cell wall (Figure 5K). In larger trichomes, most of the PD across the wall face showed strong MP-GFP labeling. In many of these trichomes, the GFP signal did not always overlay precisely with the calreticulin signal (e.g., Figure 5K), possibly due to the different planes of localization of these proteins, with calreticulin exposed at the neck region of the fracture surface and MP-GFP embedded in the PD cavity. It should also be noted that antibody staining and MP-GFP fluorescence is absent from the regions of wall directly above perpendicular epidermal cell walls (Figures 5J, 5L, and 5M), suggesting that PDs are removed or displaced when a new adjoining wall is formed.

A Computational Model of Secondary PD Formation (Plasmodesmap)

Based on our observations of multiple PD twinning events, we developed a computational model (Plasmodesmap) that predicts the distribution of PD during radial wall extension. Our model assumes that (1) the initial appearance of twinned PD occurs radially, as observed in wall fractures, with subsequent new PD occurring successively at right angles to the direction of insertion of the preceding PD; (2) the probability of new PD insertion increases linearly with the radial distance from the center of the cell plate; and (3) the cell plate undergoes a smooth transition from exponential to faster-than-exponential expansion as the plate approaches its final size (see computational methods for further details). The model is characterized by six basic parameters: the initial and final cell plate radii, the transition radius at which growth becomes faster than exponential, the rate of expansion of the cell plate, the initial PD density, and a parameter controlling the rate at which insertion probability increases with radial distance. Adjustment

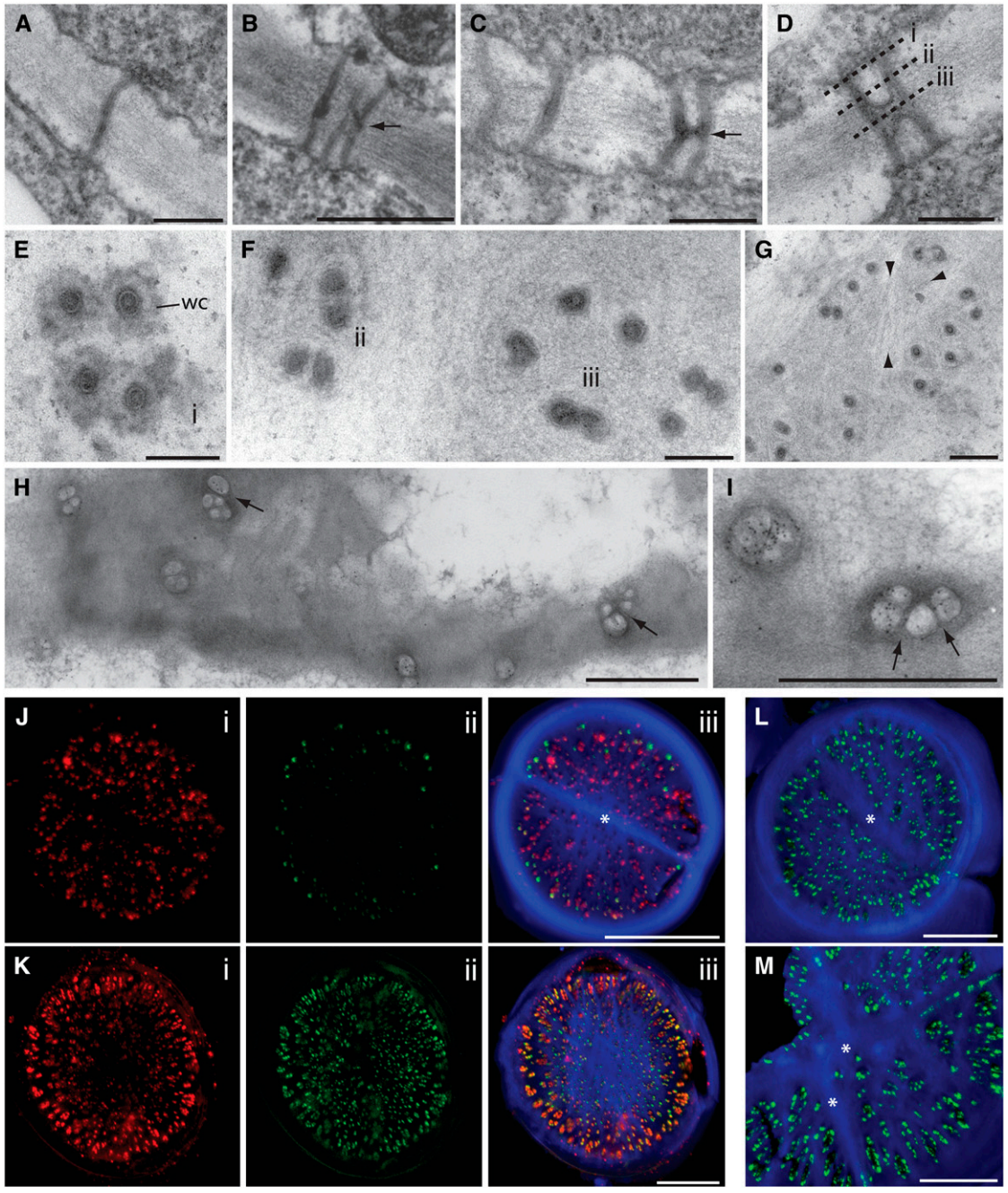

Figure 5. TEM and Immunolabeling of PD.

(A) Transmission electron micrograph showing a simple PD pore in an immature trichome wall. Bar = 0.2 μm.
(B) and **(C)** Development of H-shaped intermediates between adjacent PD pores (arrows). Bars = 0.5 μm in **(B)** and 0.2 μm in **(C)**.
(D) Development of a central cavity between two adjacent pores. The regions (i), (ii), and (iii) depict the neck region, mid wall, and central cavity regions, respectively. Bar = 0.2 μm.
(E) Section through the neck region of PD pores showing wall collars (wc) corresponding to region (i) in **(D)**. Note the elongated appearance of some of the pores. Bar = 0.1 μm.
(F) Oblique section near mid region of wall showing areas similar to (ii) and (iii) in **(D)**. Bar = 0.1 μm.
(G) Oblique section of pit field showing cellulose microfibrils (arrowheads) separating groups of PD (cf. Figures 4B and 4C). Bar = 0.2 μm.
(H) Glancing section through the mid wall region of pit fields showing extensive central cavities. Note that the central cavities are separated by distinct septa (arrows), giving them a segmented appearance in transverse section. Bar = 1.5 μm.
(I) Enlargement of two central cavities showing strong immunogold labeling of MP-GFP. Wall septa are indicated (arrows). Bar = 1.5 μm.
(J) and **(K)** Centripetal targeting of PD by MP-GFP (i, calreticulin antibody, red; ii, MP-GFP, green; iii, counterstainng with calcofluor, blue). In **(J)**, the underlying epidermal cell has divided (asterisk) but MP-GFP targeting has just initiated. In **(K)**, MP-GFP targeting of PD is complete and GFP and calreticulin signals mostly overlap. Bars = 10 μm.
(L) and **(M)** Absence of MP-GFP labeling in regions of wall in which epidermal cell walls have fused with the trichome wall (asterisks). Bars = 10 μm.

of these parameters to fit local PD density profiles (see Supplemental Figure 2 online) gave rise to PD pit field patterns very similar to those observed in fractured cell walls. The start and end points of a simulation in which the cell wall extended from 9 to 45 μm in diameter are shown in Figure 6A. The complete simulation, showing the formation of pit fields from individual primary PD is shown in Supplemental Movie 1 online. Consistent with what we observed in planta, the model generated pit fields of increasing size with increasing distance from the center of the postcytokinetic wall (Figures 6A and 6C). The radial PD patterns generated by the model, showing the early stages of progeny formation, were strikingly similar to those observed on fractured wall faces in which wall extension had been initiated (Figure 6D). In addition, the model was able to track the fate of individual primary PD and their progeny during radial wall extension. A simulation of pit field development from a primary PD progenitor is shown in Figure 6B and Supplemental Movie 2 online. Note that at the end of the period of wall extension, primary PD may become separated from their progeny by considerable distances. Also, progeny derived from the same primary PD pore may become separated spatially into two distinct groups.

DISCUSSION

In higher plants, the origin of primary PD from entrapped ER strands at cytokinesis is well established (Hepler, 1982; reviewed in Roberts and Oparka, 2003). The origin of secondary PD is less clear (Roberts, 2005). Our current data, employing a range of imaging approaches, indicate that secondary PD arise in direct contact with existing PD during radial wall extension. Existing PD continue to function as templates for the insertion of new PD, giving rise to multiply paired PD within a pit field. Thus, not all secondary PD arise simultaneously during wall development, but rather from a progressive deposition of new pores that may be linked to the rate of wall extension. In the trichome basal cell wall, the total number of PD increased fivefold during wall extension due to the insertion of new secondary PD. We found that the density of PD (per μm^{-2} of cell wall) declined during wall extension. If all the primary PD had acted as templates for new PD, the total numbers of PD would have risen exponentially. The observed increase in the total number of PD as trichome diameter increased is consistent with a model in which the outermost PD of the wall more frequently give rise to secondary PD. Indeed, our observations of fractured walls revealed that many of the primary PD pores in the central region of expanding cell walls remained as single pores (see Figure 3C). We noticed that the twinning of PD was highly synchronized, with many of the twinned PD appearing to be caught at the same stage of formation in the fractured wall face (Figures 2D and 2E). The factors underlying the synchronized behavior of these PD remain to be determined.

Interestingly, in one of the earliest EM studies of PD, Krull (1960) noticed discrete pairs of PD in shared wall interfaces between *Viscum album* cells. She referred to these as doppelröhren (double tube) structures and proposed that PD might be able to divide longitudinally, a view met with skepticism (reviewed in Robards, 1975). It is now more commonly accepted that branched PD arise from the initial fusion of adjacent existing primary PD (Ding et al., 1992a; Ding and Lucas, 1996; Ehlers and Kollmann, 2001), followed by the addition of new channels that become connected to the original pore by a process of localized wall erosion (Ding and Lucas, 1996; Ehlers and Kollmann, 2001). Our study is a comprehensive view of PD development across a single shared wall interface.

The Pattern of Secondary PD Development

It could be argued that the paired PD profiles we observed could be viewed as fusion profiles of neighboring primary PD that merged within the cellulose wall. However, we found no evidence for migration of primary PD, which would have been manifest by PD appearing in increasingly closer proximity to one another during radial wall extension and no evidence for selective removal of primary PD (see Burgess, 1971). The observation of PD twins and more complex groups toward the cell periphery suggests that a subset of the outer primary PD became templates for new pores and that the process continued during wall extension. In our model, all PD in a pit field are related and derived from a single primary PD progenitor that was incorporated into the expanding pit field along with its own progeny. Our methods do not allow us to track the fate of individual primary versus secondary PD noninvasively, although this might be achieved in the near future by the use of specific probes that mark both classes of PD separately (Oparka and Boevink, 2005).

The hypothesis that primary PD function as templates for the formation of new PD is supported by our simulation model, Plasmodesmap, which generated pit fields with a striking resemblance to those seen in freeze-fractured walls based on the probability that peripheral primary PD are more likely to produce new PD pores than those at the center of the cell plate, a feature we observed routinely in fractured cell walls.

Formation of Central Cavities

As new PD pores are inserted into the wall they become progressively connected in the region of the middle lamella by a lateral branch that extends into a cavity. Eventually, subsets of pores within a pit field become connected to a central cavity, with each cavity separated by thin wall septa. These septa are possibly derived from the same oblique cellulose bands that subdivide the pit fields into discrete units (Figures 4D and 4E). It is clear that MP-GFP targeting of central cavities, a general feature of branched PD formation (Figure 5; Roberts and Oparka, 2003), occurs relatively late in the extension of the cell wall, proceeding in a centripetal wave toward the center of the cell. At present, we are unable to determine whether MP targeting is dependent on the cavities reaching a critical size or whether MP targeting reflects a functional change in the properties of the secondary PD. While the significance of the enlarged central cavity for intercellular communication in plants is unknown, it has been suggested that one or more kinases responsible for MP phosphorylation may reside within the central cavities of branched PD (Citovsky et al., 1993; Ding, 1998). Isolation of the proteins specifically associated with branched PD (Kishi-Kaboshi et al., 2005) may yield new information on the function of these unique structures.

How Are New PD Formed?

Our observations are consistent with a model in which new secondary PD pores are being continuously inserted into existing

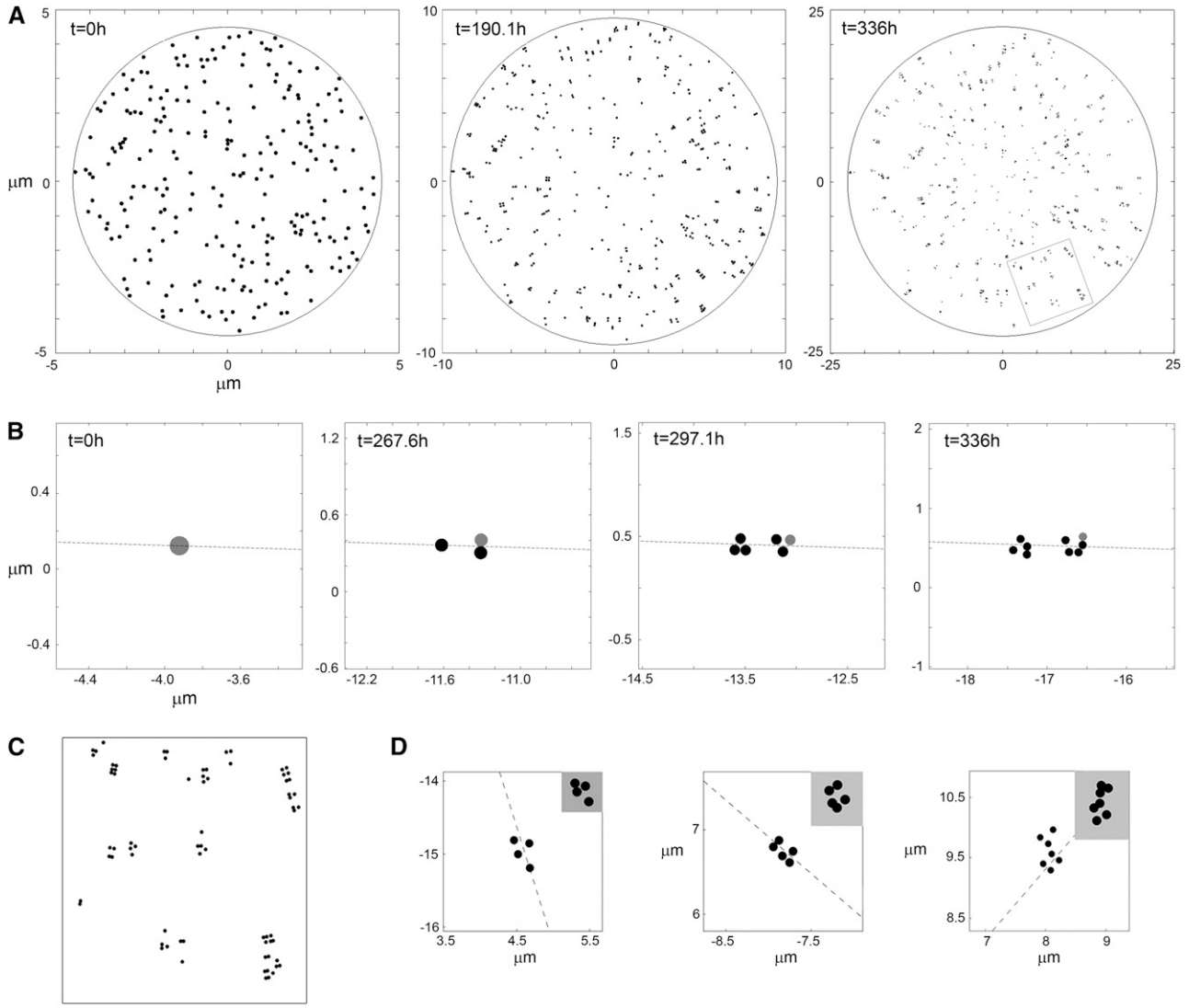

Figure 6. Simulation Modeling of Secondary PD Formation.

(A) The postcytokinetic wall is randomly seeded with PD at a distribution of 4 PD μm^2 of wall at time = 0 h to generate the first frame of the Plasmodesmap simulation. The next two frames are at time point t = 190.1 h and t = 336 h, the endpoint of the simulation. Axes indicate the spatial coordinates of the trichome wall in micrometers with (0, 0) being the center. The boxed area is enlarged in **(C)**. For full simulation, see Supplemental Movie 1 online.

(B) Four time points (t = 0 h, t = 267.6 h, t = 297.1 h, and t = 336 h) from the Plasmodesmap simulation show the generation of two distinct pit fields from a single progenitor PD. Axes indicate the distance from the center of the trichome wall in micrometers, and the broken line represents the radius of the wall. For full simulation, see Supplemental Movie 2 online.

(C) As the wall extends from 9 to 45 μm in diameter, secondary PD arise from fissions of existing PD, giving rise to discrete pit fields as seen in this enlargement of the boxed region of **(A)** (t = 336 h).

(D) Plasmodesmap-generated PD clusters that bear a striking resemblance to PD formations seen in fractured wall faces (insets). The graphs are representations of PD formations generated by the computer simulation Plasmodesmap with the axes again indicating the distance from the center of the cell wall in micrometers and the broken line representing the radius of the wall. The insets are PD formations that were observed in scanning electron micrographs of fractured trichome basal cell walls.

pectin-rich pit fields as the pit fields enlarge. From a spatial point of view, inserting new PD immediately adjacent to existing PD would maintain an ordered pattern of PD development because the template for PD formation is effectively copied at each successive insertion within a pit field. It is possible that the machinery necessary to create a new PD pore is already located in or around existing PD. Furthermore, the gel-like nature of the pectin surrounding PD (Willats et al., 2001; Cosgrove, 2005) would allow the incorporation of new PD without a major disturbance to the existing cell wall architecture. Within the extending

wall, various PD profiles were found that we interpret as intermediates leading to the formation of PD pairs (Figure 7). In some cases, the primary PD pores were elongated in the radial plane and contained paired membranous structures, possibly desmotubules, within the same pore (Figure 7). In others, the pores showed a central partition between them, while the collars appeared to be one continuous structure. We also found profiles in which the wall collars appeared to be separating and yet others in which the two pores were clearly separated but remained touching. Finally, we found closely associated PD derivatives in which the wall collars were clearly separated by intervening cellulose microfibrils. These profiles are also shown diagrammatically in Figure 7. With progressive extension of the tobacco trichome basal wall, the twinned pores become connected by a central cavity (Figure 7A), although it should be noted that in some species not all PD in a pit field become connected by central cavities (Roberts, 2005; Figure 7A).

It is possible that PD might be able to divide longitudinally, as originally suggested by Krull (1960). Several of the paired profiles we observed shared the same wall collars, indicating that the new pore may have been derived by fission of the original pore. A new ER strand is then inserted into an elongated pore to form a second desmotubule (Figure 7A). Interestingly, the presence of two desmotubules within a single PD pore has been reported previously during secondary PD formation in Strasburger cells (Glockmann and Kollmann, 1996).

An alternative scenario is that each new PD pore is inserted into the existing cell wall immediately adjacent to the original pore by selective removal of the cell wall (Figure 7B). The cortical ER may insert into the expanding wall tunnel to derive the

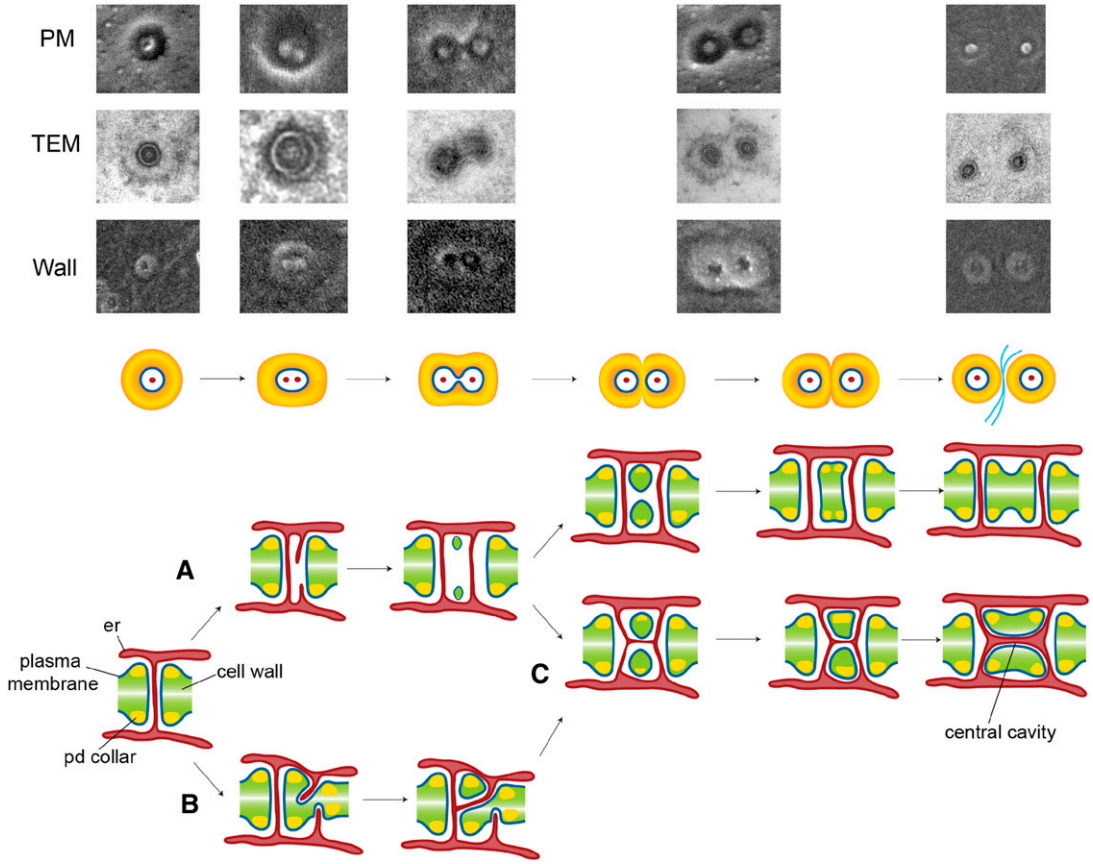

Figure 7. Models of Secondary PD Formation.

The top images show, from top to bottom, the PM fracture plane, TEM images of the neck region, and the wall fracture plane for putative stages in the formation of secondary PD pores.

(A) Fission model. The diagram depicts the insertion of a second desmotubule into an elongated PD pore, creating two desmotubules within a shared pore orifice. With increasing wall extension, the new PD becomes separated from the original by increasing deposition of new wall microfibrils between the two pores. Central cavities may or may not form between the two pores, depending on the plant species in question (top and bottom panels).

(B) De novo pore formation. The new PD pore is inserted immediately adjacent to the template pore by localized erosion of the cell wall. Two new desmotubules, each originating from a different cell, merge in the middle lamella region of the wall to form a complex structure.

(C) Branched PD formation may result from either the fission model **(A)** or de novo pore formation **(B)**. Twinned pores may or may not remain connected by ER in the middle lamella region of wall. Central cavities develop between interconnected PD as new pores are being formed.

desmotubule of the new pore (Figure 7B). The presence of multiply paired PD profiles on both the upper wall and PM surface of the adjoining cell suggests that this process must be initiated simultaneously between adjacent cells. The two extending pores then meet and fuse in the middle lamella region of the wall and may fuse with the original pore to derive a complex structure with two openings that lead into each adjoining cell (Figure 7B). Unfortunately, static electron micrographs are unable to distinguish unequivocally between the above models of secondary PD formation, although de novo insertion of a new pore by wall erosion cannot reproduce the shared pore configuration seen frequently in extending walls (Figure 7A). However, it is clear that new PD pore formation occurs in direct contact with existing PD. Our simulation model does not distinguish between the above scenarios (division versus de novo insertion), requiring only that each new PD arises in contact with an existing one to predict subsequent pit field patterning.

Our observations of multiply paired PD suggest a dynamic process in which the cortical ER is constantly being remodeled to form new desmotubules as well as fusing to form connections between individual pores. We suggest that unique classes of proteins, such as reticulons, specifically involved in ER remodeling (Voeltz et al., 2006), may be associated with the events that lead to secondary PD formation. The highly dynamic nature of PD during wall extension may also explain the fact that the PD size exclusion limit varies dramatically in developing plant tissues (Itaya et al., 1998; Oparka et al., 1999; Crawford and Zambryski, 2000; Kobayashi et al., 2005). It will be interesting to determine if the microfibril rearrangements observed during subdivision of pit fields are preceded by a shift in cortical microtubule arrays (see Lucas and Shaw, 2008) during secondary PD formation.

What Regulates the Formation of Secondary PD?

Secondary PD formation appears to be a distinctive feature of higher plant development (Seagull, 1983) and may relate to the indeterminate growth of many plant organs (Gunning, 1978). Interestingly, paired PD profiles similar to those shown here have frequently been reported in the literature, often without comment as to their origin (e.g., see images in Krull, 1960; Olesen, 1979; Seagull, 1983; Erwee and Goodwin, 1985; Barnett, 1987; Ding et al., 1992a; Itaya et al., 1998; Oparka et al., 1999; Ehlers and Kollmann, 2001), suggesting that PD twinning may be widespread among higher plants. It is likely that our present fracturing technique provides extensive views of walls that have only been seen previously in fleeting glances. Little is known of the genetic regulation of secondary PD formation or the regulation of PD branching. Kobayashi et al. (2007) recently identified an *Arabidopsis thaliana* mutant (*INCREASED SIZE EXCLUSION LIMIT2* [*ISE2*]) that developed large numbers of branched PD in the embryo, unlike the wild-type controls that contained only simple PD. The absence of the ISE2 protein (a DEVH-box RNA helicase) affects a critical factor required for correct PD development. In addition, the formation of secondary PD is enhanced in meristems by the addition of the hormone cytokinin (Ormenese et al., 2006) and is arrested in plants overexpressing an apoplastic yeast acid invertase (Ding et al., 1993). It seems likely that the extending cell wall might respond to a number of extracellular cues, such as radial stretching forces that feed back on secondary PD formation.

Future Prospects

The technique presented in this study is easy to conduct, allows correlative CLSM and FESEM imaging of PD over extensive areas of wall, and facilitates counterstaining of the cell wall around PD. A major advantage of the technique is the ability to expose, in surface view, the neck region of PD, a site where the regulation of PD aperture is thought to occur (Oparka, 2004) and where several regulatory proteins, including cytoskeletal elements, are located (Overall and Blackman, 1996). The rapid freezing protocol adopted here probably reveals the neck region of PD in close to its functioning state (see also Ding et al., 1992b). In the future, it will be interesting to view high-resolution FESEM images of the neck regions of PD in trichomes treated with reagents such as cytochalasin D that are known to interfere with the PD size exclusion limit (Ding et al., 1996) as well as in cells invaded by viruses. The ability to examine both the structure and function of PD with a single wall interface should lead to further insights into the regulation of PD conductance in plants.

METHODS

Plant Material

Nicotiana tabacum cv Xanthi plants expressing MP-GFP (Roberts et al., 2001) and *N. tabacum* cv Xanthi NN were grown from seed in a heated glasshouse and used for experiments between 20 and 60 d old. Young leaves between 1.5 and 3 cm in length were used for analysis.

Fluorescence Microscopy and Immunolocalization

For imaging GFP and counterstaining the cell wall, leaf segments were frozen in liquid nitrogen, and the trichomes were fractured by gently brushing the adaxial surface of the leaf with a scalpel blade. For immunofluorescence, leaf segments were fixed in 2% glutaraldehyde and 1% paraformaldehyde. The tissue was washed in PBS, and the trichomes were fractured as described. The leaf segments were allowed to thaw in blocking buffer (3% BSA in PBS) for 30 min and then incubated in primary antibodies overnight. After washing in PBS with 3% BSA, the segments were incubated in secondary antibodies, washed with PBS, briefly incubated in 17 μg mL^{-1} calcofluor white, and mounted with the fractured surface upwards in citifluor (Agar Scientific). Primary antibodies used were rabbit anticalreticulin (Napier et al., 1995), mouse anticallose (Biosupplies), and goat anti-(1$\rightarrow$5)-α-L-arabinan (Willats et al., 1998). Secondary antibodies were anti-rabbit conjugated to Cy3 (Sigma-Aldrich), anti-mouse conjugated to Cy3 (Sigma), and anti-goat conjugated to fluorescein isothiocyanate (Sigma-Aldrich).

The tissue was imaged using a Leica SP2 confocal laser scanning microscope (Leica Microsystems) with either a $\times$63 water-dipping lens or a $\times$63 water immersion lens (HCX PLAPO CS; Leica Microsystems). Calcofluor white was excited at 405 nm, GFP and fluorescein isothiocyanate at 488 nm, and Cy3 at 561 nm.

Low-Temperature Scanning Electron Microscopy

Whole leaves or leaf segments $\sim$2 cm long by 1 cm wide were mounted either flat, adaxial surface uppermost, on a modified Gatan cryospecimen carrier using colloidal graphite (Agar Scientific G303) as a cryo-adhesive

or by immersing the adaxial surface into the colloidal graphite. Specimens were cryofixed by plunging into melting nitrogen at about −210°C . The specimen carrier was transferred under low vacuum to the specimen stage of a Gatan Alto 2500 cryopreparation unit at about −185°C. The trichomes were fractured using a Swann Morton 10A scalpel blade that had been cooled by contact with the stage (~−185°C). The fractured specimens were sputter coated with 6 to 8 nm of 60:40 gold:palladium alloy (Testbourne) in an atmosphere of argon gas (Messer UK) and transferred under high vacuum to the cryospecimen stage of a Hitachi 4700 II cold field-emission scanning electron microscope (Hitachi High Technologies) at <−170°C. Specimens were examined at nominal image magnifications up to ×50,000 using a beam accelerating voltage of 5.0 kV, filament current of 10 μA, and working distances between 4 and 12 mm. Digital images were captured at a resolution of 2560 × 1920 pixels using the signal from the upper (semi in-lens) secondary electron detector.

TEM

Leaves of 1 to 3 cm length were fixed in 1% glutaraldehyde and 1% paraformaldehyde. Fixed tissue was postfixed in either 1% osmium tetroxide for 2 h for conventional TEM or with ZIO solution, a stain that shows affinity for the endomembrane system (for details, see Hawes et al., 1981). Samples were dehydrated through a graded ethanol series (10 to 100% anhydrous), embedded in London Resin (LR White), and polymerized overnight at 60°C. Thin sections were viewed in a Philips BioTwin transmission electron microscope. Immunogold labeling of MP-GFP was performed using antibodies to GFP as described by Escobar et al. (2003).

Calculation of PD Densities and Distributions

FESEM images were collected from selected areas of fractured trichomes. The area imaged for each trichome included the center of the trichome and radial planes in at least two directions from the center to the edge. Individual images were montaged using Adobe Photoshop (Adobe Systems). The diameter and area imaged for each trichome were calculated using Image J (National Institutes of Health), and these figures were used to calculate the total wall area of the trichome and PD densities. Concentric circles with increasing radii of 2.5 μm were overlayed on the montaged images, and the number of discrete PD and those with collars that touched at least one other PD were counted.

Computational Methods

Plasmodesmap: A Simulation Model of Pit Field Formation

The hypothesis that secondary PD arise from fissions of primary PD was tested using an agent-based computational model (Walker et al., 2004; Cannata et al., 2005; Christley et al., 2007). Individual PD were modeled as autonomous agents situated within an expanding circular disk, representing the cell plate. The insertion of a new plasmodesma was assumed to occur either along the radial line of the parent plasmodesma or perpendicular to this line, depending on whether the parent itself had arisen from a radial or perpendicular insertion. PD arising from radial insertions were assumed to subsequently undergo perpendicular insertions and vice versa.

The state of each agent at time t (h) was described by three variables: its polar coordinates $[r(t),\theta(t)]$ and a binary variable m_D, which recorded whether it was the product of a radial insertion ($m_D = +1$) or a perpendicular one ($m_D = -1$). The insertion of new PD was modeled as an inhomogeneous Poisson process with rate $\lambda r(t)$. This ensured that the probability of insertion was an increasing function of radial distance, yielding the simplest probability model consistent with the assumption that PD near the periphery of the plate are more likely to produce new PD pores than those closer to the center. Insertions were not allowed to occur if the resulting plasmodesma overlapped with existing ones. Writing r_P for the radius of a plasmodesma, the update rule for each agent can be expressed concisely as

$$(r(t),\theta(t),m_D)\mapsto \begin{matrix}\big(f_1(G_{(\mu,\Delta t)}(r(t))),g_1(G_{(\mu,\Delta t)}(r(t)),\theta(t)),-m_D\big)\\ \big(f_2(G_{(\mu,\Delta t)}(r(t))),g_2(G_{(\mu,\Delta t)}(r(t)),\theta(t)),-m_D\big)\end{matrix} \quad (1)$$

where

$$f_1(r)=f_2(r)=\sqrt{r^2+{r_P}^2} \quad \text{if } m_D=+1$$
$$g_1(r,\theta)=\theta-\arctan(r_P/r),\ g_2(r,\theta)=\theta+\arctan(r_P/r)$$

$$f_1(r)=r-r_P,\ f_2(r)=r+r_P \quad \text{if } m_D=-1$$
$$g_1(r,\theta)=g_2(r,\theta)=\theta$$

and Δt denotes the time of the next insertion. In the above, the function $G_{(\mu,\Delta t)}(r)$ represents the growth of the plate at radius r over the time interval Δt, parameterized by an expansion rate μ (see below).

Initial Conditions and Parameter Values

Simulations were initialized by randomly distributing agents over a disk of radius R_0 according to an initial PD density ρ. For all agents in the initial distribution, m_D was set equal to −1 so that the first fission would be radial. Agents were then updated according to Equation 1 until the radius of the plate edge reached a target value R_1.

Initially, it was assumed that the rate of change dr/dt of disk expansion was simply linearly proportional to radius r, giving $dr/dt = \mu r$. This results in pure exponential growth of the disk, corresponding to setting $G_{(\mu,\Delta t)}(r) = e^{\mu\Delta t} r$ in Equation 1. R_1 was varied between 5 and 50 μm, covering the range of trichomes analyzed experimentally, while R_0 was varied about the value $0.2R_1$. The cell plate expansion rate μ was set close to 0.005 h^{-1} so as to give run times close to 336 h, while ρ was varied from 2.5 $(\mu m)^{-2}$ on the basis of PD densities computed from the trichomes of smallest diameter. By changing the fission probability λ between 0.0001 and 0.001, PD distributions with pit field patterns qualitatively similar to experimental ones were obtained. However, these simulated distributions were unable to reproduce changes in local PD density, as assessed by dividing the plate into *N* concentric circles of increasing radius 2.5 μm apart and computing the PD density $\{\delta_1,\ldots,\delta_N\}$ within each resulting annulus of width 2.5 μm bounded by the circles. The experimental local density profiles computed in this manner showed a characteristic increase in density with increasing concentric circle radius, followed by a drop as the edge of the plate was approached (see Supplemental Figure 2 online). By contrast, the model yielded monotonically increasing profiles for all parameter sets tried.

The inability of exponential cell plate expansion to reproduce experimental local density profiles suggested modifying the model to one in which the expansion rate becomes faster than exponential as the edge of the plate approaches R_1 so as to give a lower comparative density at the periphery. The simplest such model incorporating this effect was obtained by setting $dr/dt = (\mu/2R_0)r^2$, corresponding to $G_{(\mu,\Delta t)}(r) = r/(1-(\mu/2R_0)r\Delta t)$ in Equation 1. This second model produced local density profiles that decreased monotonically with increasing radius, again inconsistent with experimental results. However, profiles consistent with experimental data were obtained with a third, combined model in which growth was assumed to be exponential below a given threshold

radius r_T ($<R_1$) and faster than exponential beyond r_T ($dr/dt = \mu r$ for $r<r_T$ and $dr/dt = (\mu/2R_T)r^2$ for $r>r_T$, equivalent to $G_{(\mu,\Delta t)}(r) = e^{\mu\Delta t} r$ for $r<r_T$ and $G_{(\mu,\Delta t)}(r) = r/(1-(\mu/2R_T)r\Delta t)$ in Equation 1. Furthermore, by tuning the parameters of this combined model appropriately (starting from values used in the initial pure exponential growth model), good matches could be obtained to experimental local density profiles (see Supplemental Figure 2 online). The goodness-of-fit measure used for this tuning procedure was the root mean square (RMS) difference d_{RMS} between the experimental and simulated profiles, $\{\delta_1{}^E,\ldots,\delta_N{}^E\}$ and $\{\delta_1{}^S,\ldots,\delta_N{}^S\}$:

$$d_{RMS} = \sqrt{\frac{1}{N}\sum_{i=1}^{N}(\delta_i{}^E - \delta_i{}^S)^2}.$$

The parameter set yielding the smallest value of d_{RMS} was taken as most representative of data and was used to generate the other PD patterns shown in this work (parameter values are given in the caption to Supplemental Figure 2A online).

Model Software

Matlab code for the model, including routines for producing movies, can be obtained by request from oakman@staffmail.ed.ac.uk.

Supplemental Data

The following materials are available in the online version of this article.

Supplemental Figure 1. Enlargement of the Basal Trichome Cell Wall Is Accompanied by Asymmetric Divisions in the Underlying Epidermal Cells.

Supplemental Figure 2. Experimental and Simulated Local Density Profiles Computed from PD Distributions between Concentric Circles of Increasing Radius 2.5 μm Apart.

Supplemental Movie 1. Simulation of PD Insertion during Wall Expansion Generated by Plasmodesmap, Showing Enlargement of the Basal Cell Wall from 9 to 45 μm in Diameter, Accompanied by the Formation of Radial Pit Fields.

Supplemental Movie 2. Plasmodesmap Simulation of the Insertion of New PD to Produce Secondary PD within Pit Fields.

ACKNOWLEDGMENTS

We thank Steve Mitchell for his help with the electron microscopy, Paul Knox for providing the LM6 antibody, and Richard Napier for providing the anticalreticulin antibody.

Received November 13, 2007; revised May 28, 2008; accepted June 12, 2008; published June 30, 2008.

REFERENCES

Angell, S.M., Davies, C., and Baulcombe, D.C. (1996). Cell-to-cell movement of potato virus X is associated with a change in the size exclusion limit of plasmodesmata in trichome cells of *Nicotiana clevelandii.* Virology **216:** 197–201.

Badelt, K., White, R.G., Overall, R.L., and Vesk, M. (1994). Ultrastructural specialisations of the wall sleeve around plasmodesmata. Am. J. Bot. **81:** 1422–1477.

Baluska, F., Samaj, J., Napier, R., and Volkmann, D. (1999). Maize calreticulin localizes preferentially to plasmodesmata in root apex. Plant J. **14:** 481–488.

Barnett, J.R. (1987). Changes in the distribution of plasmodesmata in developing fibre-tracheid pit membranes of *Sorbus aucuparia* L. Ann. Bot. (Lond.) **59:** 269–279.

Baskin, T. (2005). Anisotropic expansion of the plant cell wall. Annu. Rev. Cell Dev. Biol. **21:** 203–222.

Burgess, J. (1971). The occurrence of plasmodesmata-like structures in a non-division wall. Protoplasma **74:** 449–458.

Cannata, N., Corradini, F., Merelli, E., Omicini, A., and Ricci, A. (2005). An agent-oriented conceptual framework for systems biology. Trans. Comput. Syst. Biol. **3:** 105–122.

Christley, S., Alber, M.S., and Newman, S.A. (2007). Patterns of mesenchymal condensation in a multiscale, discrete stochastic model. PLoS Comput. Biol. **3:** e76.

Citovsky, V., McLean, B.G., Zupan, J.R., and Zambryski, P. (1993). Phosphorylation of tobacco mosaic virus cell-to-cell movement protein by a developmentally regulated plant cell wall-associated protein kinase. Genes Dev. **7:** 904–910.

Cosgrove, D.J. (2005). Growth of the plant cell wall. Nat. Rev. Mol. Cell Biol. **6:** 850–861.

Crawford, K.M., and Zambryski, P.C. (2000). Subcellular localization determines the availability of non-targeted proteins to plasmodesmatal transport. Curr. Biol. **10:** 1032–1040.

Derrick, P.M., Barker, H., and Oparka, K.J. (1992). Increase in plasmodesmatal permeability during cell-to-cell spread of tobacco rattle virus from individually inoculated cells. Plant Cell **4:** 1405–1412.

Ding, B. (1998). Intercellular protein trafficking through plasmodesmata. Plant Mol. Biol. **38:** 279–310.

Ding, B., Haudenshield, J.S., Hull, R.J., Wolf, S., Beachy, R.N., and Lucas, W.J. (1992a). Secondary plasmodesmata are specific sites of localization of the tobacco mosaic virus movement protein in transgenic tobacco plants. Plant Cell **4:** 915–928.

Ding, B., Haudenshield, J.S., Hull, R.J., Wolf, S., Beachy, R.N., and Lucas, W.J. (1993). Correlation between arrested secondary plasmodesmata development and onset of accelerated leaf senescence in yeast acid invertase transgenic tobacco plants. Plant J. **4:** 179–189.

Ding, B., Kwon, M.O., and Warnberg, L. (1996). Evidence that actin filaments are involved in controlling the permeability of plasmodesmata in tobacco mesophyll. Plant J. **10:** 157–164.

Ding, B., and Lucas, W.J. (1996). Secondary plasmodesmata: Biogenesis, special functions, and evolution. In Membranes: Specialised Functions in Plants, M. Smallwood, P. Knox, and D. Bowles, eds (Oxford, UK: BIOS Scientific Publishers), pp. 489–506.

Ding, B., Turgeon, R., and Parthasarathy, M.V. (1992b). Substructure of freeze-substituted plasmodesmata. Protoplasma **169:** 28–41.

Ehlers, K., and Kollmann, R. (2001). Primary and secondary plasmodesmata: structure, origin and functioning. Protoplasma **216:** 1–30.

Erwee, M.G., and Goodwin, P.B. (1985). Symplast domains in extrastelar tissues of Egeria densa. Planta **163:** 9–19.

Escobar, N.M., Haupt, S., Thow, G., Boevink, P., Chapman, S., and Oparka, K. (2003). High-throughput viral expression of cDNA–green fluorescent protein fusions reveals novel subcellular addresses and identifies unique proteins that interact with plasmodesmata. Plant Cell **15:** 1507–1523.

Faulkner, C.R., Blackman, L.M., Cordwell, S.J., and Overall, R.L. (2005). Proteomic identification of putative plasmodesmatal proteins from *Chara corallina*. Proteomcs **5:** 2866–2875.

Glockmann, C., and Kollmann, R. (1996). Structure and development of cell connections in phloem cells of *Metasequoia glyptostroboides* needles I: Ultrastructure of the modified primary plasmodesmata in Strasburger cells. Protoplasma **193:** 191–203.

Glover, B.J., and Martin, C. (2000). Specification if epidermal cell morphology. Adv. Bot. Res. **131:** 193–217.

Gunning, B.E.S. (1978). Age-related and origin-related control of the numbers of plasmodesmata in cell walls of developing *Azolla* roots. Planta **143:** 181–190.

Hawes, C.R., Juniper, B.E., and Horne, J.C. (1981). Low and high voltage electron microscopy of mitosis and cytokinesis in maize roots. Planta **152:** 397–407.

Hepler, P.K. (1982). Endoplasmic reticulum in the formation of cell plate and plasmodesmata. Protoplasma **111:** 121–133.

Itaya, A., Woo, Y.-M., Masuta, C., Bao, Y., Nelson, R.S., and Ding, B. (1998). Developmental regulation of intercellular protein trafficking through plasmodesmata in tobacco leaf epidermis. Plant Physiol. **118:** 373–385.

Kishi-Kaboshi, M., Murata, T., Hasebe, M., and Watanabe, Y. (2005). An extraction method for tobacco mosaic virus movement protein localizing in plasmodesmata. Protoplasma **225:** 85–92.

Kobayashi, K., Kim, I., Cho, E., and Zambryski, P. (2005). Plasmodesmata and plant morphogenesis. In Annual Plant Reviews, Vol. 18, K.J. Oparka, ed (Oxford, UK: Blackwell Publishing), pp. 90–116.

Kobayashi, K., Otegui, M., Krishnakumar, S., Mindrinos, M., and Zambryski, P. (2007). *Increased Size Exclusion Limit2* encodes a putative DEVH box RNA helicase involved in plasmodesmata function during *Arabidopsis* embryogenesis. Plant Cell **19:** 1885–1897.

Krull, R. (1960). Untersuchungen uber den bau und die entwicklung de plasmodesmen im rindenparenchym von *Viscum album.* Planta **55:** 598–629.

Levy, A., Erlanger, M., Rosenthal, M., and Epel, B.L. (2007). A plasmodesmata-associated beta-1,3-glucanase in Arabidopsis. Plant J. **49:** 669–682.

Lucas, J., and Shaw, S.L. (2008). Cortical microtubule arrays in the *Arabidopsis* seedling. Curr. Opin. Plant Biol. **11:** 94–98.

Lucas, W.J. (2006). Viral movement proteins: Agents for cell-to-cell trafficking of viral genomes. Virology **344:** 169–184.

Lucas, W.J., and Lee, J.-Y. (2004). Plasmodesmata as a supracellular control network in plants. Nat. Rev. Mol. Cell Biol. **5:** 712–726.

Napier, R.M., Trueman, S., Henderson, J., Boyce, J.M., Hawes, C., Fricker, M.D., and Venis, M.A. (1995). Purification, sequencing and functions of calreticulin from maize. J. Exp. Bot. **46:** 1603–1613.

Olesen, P. (1979). The neck constriction in plasmodesmata. Evidence for a peripheral sphincter-like structure revealed by fixation with tanic acid. Planta **144:** 349–358.

Oparka, K.J. (2004). Getting the message across: How do plant cells exchange macromolecular complexes. Trends Plant Sci. **9:** 33–40.

Oparka, K.J., and Boevink, P. (2005). Techniques for imaging intercellular transport. In Plasmodesmata: Annual Plant Reviews, K.J. Oparka, ed (Oxford, UK: Blackwell Publishing), pp. 241–262.

Oparka, K.J., and Prior, D.A.M. (1992). Direct evidence for pressure-generated closure of plasmodesmata. Plant J. **2:** 741–750.

Oparka, K.J., Prior, D.A.M., Santa Cruz, S., Padgett, H.S., and Beachy, R.N. (1997). Gating of epidermal plasmodesmata is restricted to the leading edge of of expanding infection sites of tobacco mosaic virus (TMV). Plant J. **12:** 781–789.

Oparka, K.J. Roberts, A.G., Boevink, P., Santa Cruz, S., Roberts, I., Pradel, K.S., Imlau, A., Kotlizky, G., Dauer, N., and Epel, B. (1999). Simple, but not branched, plasmodesmata alow the nonspecific trafficking of proteins in develoing tobacco leaves. Cell **97:** 743–754.

Orfila, C., and Knox, J.P. (2000). Spatial regulation of pectic polysaccharides in relation to pit fields in cell walls of tomato fruit pericarp. Plant Physiol. **122:** 775–781.

Ormenese, S., Bernier, G., and Perilleux, C. (2006). Cytokinin application to the shoot apical meristem of *Sinapis alba* enhances secondary plasmodesmata formation. Planta **224:** 1481–1484.

Overall, R.L., and Blackman, L.M. (1996). A model of the macromolecular structure of plasmodesmata. Trends Plant Sci. **1:** 307–311.

Robards, A.W. (1975). Plasmodesmata. Annu. Rev. Plant Physiol. **26:** 13–29.

Roberts, A.G. (2005). Plasmodesmal structure and development. In Plasmodesmata: Annual Plant Reviews, K.J. Oparka, ed (Oxford, UK: Blackwell Publishing), pp. 1–23.

Roberts, A.G., and Oparka, K.J. (2003). Plasmodesmata and the control of symplasmic transport. Plant Cell Environ. **26:** 103–124.

Roberts, I.M., Boevink, P., Roberts, A.G., Sauer, N., Reichel, C., and Oparka, K.J. (2001). Dynamic changes in the frequency and architecture of plasmodesmata during the sink-source transition in tobacco leaves. Protoplasma **218:** 31–44.

Robinson-Beers, K., and Evert, R.F. (1991). Fine structure of plasmodesmata in mature leaves of sugarcane. Planta **184:** 307–318.

Sagi, G., Katz, A., Guenoune-Gelbart, D., and Epel, B.L. (2005). Class I reversibly glycosylated polypeptides are plasmodesmal-associated proteins delivered to plasmodesmata via the Golgi apparatus. Plant Cell **17:** 1788–1800.

Seagull, R.W. (1983). Differences in the frequency and disposition of plasmodesmata resulting from root cell elongation. Planta **159:** 497–504.

Thomas, C.L., Bayer, E.M., Ritzenthaler, C., Fernandez-Calvino, L., and Maule, A.J. (2008). Specific targeting of a plasmodesmal protein affecting cell-to-cell communication. PLoS Biol. **6:** e7.

Turner, A., Wells, B., and Roberts, K. (1994). Plasmodesmata of maize root tips: structure and composition. J. Cell Sci. **107:** 3351–3361.

Voeltz, G.K., Prinz, W.A., Shibata, Y., Rist, J.M., and Rapaport, T.A. (2006). A class of membrane proteins shaping the tubular endoplasmic reticulum. Cell **124:** 573–586.

Waigmann, E., Turner, A., Peart, J., Roberts, K., and Zambryski, P. (1997). Ultrastructural analysis of leaf trichome plasmodesmata reveals major differences from mesophyll plasmodesmata. Planta **203:** 75–84.

Waigmann, E., and Zambryski, P. (1995). Tobacco mosaic virus movement protein-mediated protein transport between trichome cells. Plant Cell **7:** 2069–2079.

Waigmann, E., and Zambryski, P. (2000). Trichome plasmodesmata: A model system for cell-to-cell movement. Adv. Bot. Res. **31:** 261–281.

Walker, D.C., Hill, G., Wood, S.M., Smallwood, R.H., and Southgate, J. (2004). Agent-based computational modelling of epithelial cell monolayers: Predicting the effect of exogenous calcium concentrations on the rate of wound closure. IEEE Trans. Nanobioscience **3:** 153–163.

Willats, W.G.T., Marcus, S.E., and Knox, J.P. (1998). Generation of a monoclonal antibody specific to (1→5)-α-L-arabinan. Carbohydr. Res. **308:** 149–152.

Willats, W.G.T., McArtney, L., Mackie, W., and Knox, P.J. (2001). Pectin: Cell biology and prospects for functional analysis. Plant Mol. Biol. **47:** 9–27.